PLOS ONE

RESEARCH ARTICLE

Tensor framelet based iterative image reconstruction algorithm for low-dose multislice helical CT

Haewon Nam[1], Minghao Guo[2], Hengyong Yu[3], Keumsil Lee[4], Ruijiang Li[5], Bin Han[5], Lei Xing[5], Rena Lee[6], Hao Gao[7]*

1 Department of Liberal Arts, Hongik University, Sejong, Republic of Korea, **2** School of Biomedical Engineering, Shanghai Jiao Tong University, Shanghai 200240, China, **3** Department of Electrical and Computer Engineering, University of Massachusetts, Lowell, Massachusetts 01854, United States of America, **4** Department of Radiology, Stanford University, Stanford, California 94305, United States of America, **5** Department of Radiation Oncology, Stanford University, Stanford, California 94305, United States of America, **6** Department of Radiation Oncology, Ewha Womans University, Seoul, Korea, **7** Department of Radiation Oncology, Emory University, Atlanta, GA 30322, United States of America

* hao.gao.2012@gmail.com

Citation: Nam H, Guo M, Yu H, Lee K, Li R, Han B, et al. (2019) Tensor framelet based iterative image reconstruction algorithm for low-dose multislice helical CT. PLoS ONE 14(1): e0210410. https://doi.org/10.1371/journal.pone.0210410

Editor: Qinghui Zhang, North Shore Long Island Jewish Health System, UNITED STATES

Received: September 10, 2018

Accepted: December 21, 2018

Published: January 11, 2019

Data Availability Statement: All relevant data are within the manuscript and its Supporting Information files.

Funding: H. Nam was supported by the Basic Science Research program through NRF (#2015R1C1A2A01054731) of Korea funded by the ministry of Education Science and Technology. L. Xing is supported partially by NIH/NIBIB 1R01 EB-016777. R. Lee was supported by the Korea Institute for Advancement of Technology (KIAT) grant funded by the Korea government (Ministry of Trade, Industry and Energy, No.0001723).

Abstract

In this study, we investigate the feasibility of improving the imaging quality for low-dose multislice helical computed tomography (CT) via iterative reconstruction with tensor framelet (TF) regularization. TF based algorithm is a high-order generalization of isotropic total variation regularization. It is implemented on a GPU platform for a fast parallel algorithm of X-ray forward band backward projections, with the flying focal spot into account. The solution algorithm for image reconstruction is based on the alternating direction method of multipliers or the so-called split Bregman method. The proposed method is validated using the experimental data from a Siemens SOMATOM Definition 64-slice helical CT scanner, in comparison with FDK, the Katsevich and the total variation (TV) algorithm. To test the algorithm performance with low-dose data, ACR and Rando phantoms were scanned with different dosages and the data was equally undersampled with various factors. The proposed method is robust for the low-dose data with 25% undersampling factor. Quantitative metrics have demonstrated that the proposed algorithm achieves superior results over other existing methods.

Introduction

X-ray computed tomography (CT) has been one of the most widely used medical imaging techniques since Hounsfield invented the first commercial medical X-ray machine in 1972 [1]. The Helical CT was first invented by I. Mori [2] in the late 1980s and was developed by W. Kalender [3] in the 1990s. The number of detector rows has been increased to achieve larger volume coverage with a reduced scan time and improved z-resolution. The 8-slice CT system was first introduced in 2000, Siemens SOMATOM Definition scanner has 64-slice rows for up

Competing interests: The authors have declared that no competing interests exist.

to 128-channel data acquisition, and the Toshiba Aquilion ONE ViSION, which has 320-slice rows for generating 640 slices, was brought out in 2013.

Helical CT reconstruction algorithms can be categorized into two groups: Analytic reconstruction and iterative algorithm. An analytic reconstruction can be sub-divided into exact and approximate reconstruction methods. The Feldkamp-Davis-Kress algorithm (FDK) is a well-known approximate analytic reconstruction algorithm [4] and it can be generalized for helical scan trajectories [5–7]. However, FDK generates helical artifacts due to data insufficiency. A conventional filtered backprojection (FBP) algorithm can be implemented with data interpolation [8] to soften helical artifacts, but this may generate another type of artifact caused by data approximation. In 2002, Katsevich introduced an exact FBP-type reconstruction algorithm based on the PI-line and Tam-Danielsson window [9–11]. Details for the numerical implementation of the Katsevich algorithm are given in [12, 13]. An alternative derivation of the Katsevich algorithm is provided by Chen [14]. Meanwhile, another exact method of backprojection-filtration (BPF) has been developed by Zou and Pan [15], and these ideas have inspired several subsequent exact reconstruction methods [16–20].

Katsevich-type algorithms are based on exact analytic theory, and thus it is sensitive to the noisy projection data. To overcome these noise sensitivity, many researchers have studied iterative reconstruction algorithms [21, 22] by formulating the image reconstruction as an optimization problem based on versatile CT models. The Algebraic Reconstruction Technique (ART) [1, 23] and Simultaneous Algebraic Reconstruction Technique (SART) [24] are two of the most popular methods in the early stage of iterative reconstruction algorithms. Iterative reconstruction algorithms are based on a mathematical minimization which seeks the best approximate solution. They have greater flexibility, and thus are robust against noise. A regularization term, such as Tikhonov or total-variation (TV) regularizer, can be added to the cost function for noise and artifact reduction. Compared with analytic reconstruction algorithms, iterative reconstruction algorithms work well even with insufficient or low-dose data. However a significant disadvantage of iterative reconstruction is its high computational cost, particularly for helical CT scans, which contain a huge amount of data. Thanks to recent advances in computing hardware, iterative reconstruction is emerging for helical CT [21, 22, 25, 26]. Nuyts et al. [22] investigated the superiority of iterative reconstruction compared to non-iterative methods for a helical CT system. They concluded that iterative reconstruction improved the axial resolution. Thibault et al. [21] presented a Bayesian iterative reconstruction algorithm for multislice helical data, they showed improved high contrast spatial resolution and signal-to-noise ratio relative to analytic methods. Yu and Zeng [26] developed a TV-based iterative algorithm and applied it to a limited-angle inverse helical CBCT reconstruction for C-arm system.

In this article, we propose an iterative reconstruction algorithm to improve multi-slice helical CT based on tensor framelet (TF) [27, 28] regularization. The method belongs to a sparsity-regularized model-based iterative reconstruction, which is inspired by compressive sensing [29, 30]. To name a few: Sidky et al. develops a TV-based iterative method for sparse-view and limited-angle reconstruction [31]; Chen et al. proposes the so-called PICCS method for the dynamic CT problem [32]; Yu and Wang studies the sparsity-regularized method for interior tomography [33]; Gao et al. proposes a rank-sparsity decomposition method for dynamic CT [34] and spectral CT [35]; Jia et al. studies tight frame regularization for cone-beam CT image reconstruction [36]; Xu et al. develops a dictionary learning-based image reconstruction method for dose reduction [37].

This paper is organized as follows: Section II provides the materials and method details, including the minimization problem, TF regularization, optimization algorithm for iterative multislice helical CT image reconstruction, and experimental details. Section III presents the validation of the proposed method for low-dose multislice helical CT in comparison with

FDK, the Katsevich and TF algorithms, with low-dose and sparse-view data. Section IV summarizes this work.

Materials and methods

Minimization problem

The mathematical formulation of an iterative CT reconstruction can be expressed by a least-square minimization problem as

$$\mathbf{x} = \arg\min_{\mathbf{x}} \frac{1}{2}\|\mathbf{A}\mathbf{x} - \mathbf{y}\|_2^2 + \lambda R(\mathbf{x}), \tag{1}$$

where $\mathbf{x}$ is the three-dimensional image to be reconstructed with given projection data $\mathbf{y}$ and the projection matrix $\mathbf{A}$. The first term indicates the data fidelity in the L^2-norm. The second term consists of $R(\mathbf{x})$ as a regularization function with regularization parameter λ. For example, the TV norm is a popular regularization choice for sparsity-based CT image reconstruction [31, 32].

In this paper, we solve Eq (1) with the given data $\mathbf{y}$ from the multislice helical CT system. The projection matrix $\mathbf{A}$ contains the helical geometry with the flying focal spot [38]. For the forward projection $\mathbf{A}$ and its adjoint $\mathbf{A}^T$, parallelized algorithms with an infinitely narrow beam are used with GPU implementation [39].

Tensor framelet regularization. Consider a 3D image $\mathbf{x}$ as a tensor,

$$\mathbf{x} = \{x_{ijk}, i \le N_x,\ j \le N_y,\ k \le N_z\}$$

where x_{ijk} is the (i, j, k)-th voxel in three-dimensional image space, N_x, N_y, and N_z are the number of voxels in the x, y and z–axis respectively. We define $\mathbf{x}_x$, $\mathbf{x}_y$, and $\mathbf{x}_z$ as 1D unfolded matrices of $\mathbf{x}$ along the x, y, and z–axes, respectively. The TF transform is constructed using the standard $1D$ framelet transform [40], e.g., the 1D piecewise linear tight frame with the following refinement masks.

$$\omega_0 = \frac{1}{4}[1\ \ 2\ \ 1],\ \ \omega_1 = \frac{\sqrt{2}}{4}[1\ \ 0\ \ -1],\ \ \omega_2 = \frac{1}{4}[-1\ \ 2\ \ -1].$$

The operator ω_0 is an averaging operator, and the two other operators ω_1 and ω_2 are the first and second differential operators, respectively. Note that ω_0 smoothes the image, while ω_1 and ω_2 enhance the edges. Define

$$\mathbf{M}_j\mathbf{x} = \frac{1}{\sqrt{3}}\begin{bmatrix} \omega_j * \mathbf{x}_x \\ \omega_j * \mathbf{x}_y \\ \omega_j * \mathbf{x}_z \end{bmatrix}, \forall j = 0, 1, 2,$$

where $*$ denotes the convolution operator. The TF regularization function $\mathbf{W}$ and its adjoint $\mathbf{W}^T$ are respectively defined as below.

$$\mathbf{W}\mathbf{x} = [\mathbf{M}_0\mathbf{x},\ \ \mathbf{M}_1\mathbf{x},\ \ \mathbf{M}_2\mathbf{x}]^T, \tag{2}$$

and

$$\mathbf{W}^T\mathbf{y} = \mathbf{M}_0^T(\mathbf{M}_0\mathbf{x}) + \mathbf{M}_1^T(\mathbf{M}_1\mathbf{x}) + \mathbf{M}_2^T(\mathbf{M}_2\mathbf{x}),\ \ \texttt{for}\ \ \mathbf{y} = \mathbf{W}\mathbf{x}. \tag{3}$$

The TF norm is defined as $\lambda\|\mathbf{W}\mathbf{x}\|_1 = \lambda_0\|\mathbf{M}_0\mathbf{x}\|_1 + \lambda_1\|\mathbf{M}_1\mathbf{x}\|_1 + \lambda_2\|\mathbf{M}_2\mathbf{x}\|_1$, where

$\|\mathbf{M}_j\mathbf{x}\|_1 = \sqrt{|\omega_j * \mathbf{x}_x|^2 + |\omega_j * \mathbf{x}_y|^2 + |\omega_j * \mathbf{x}_z|^2}$, for all $j = 0$, 1, and 2. TF transform $\mathbf{W}$ is left invertible and $\mathbf{W}^T\mathbf{W} = I$, by the simple calculation [27]. If $\lambda_0 = 0$, $\lambda_1 \neq 0$, and $\lambda_2 = 0$, $\|\mathbf{W}\mathbf{x}\|_1$ corresponds to the isotropic TV norm of $\mathbf{x}$. In other words, TF regularization is a high-order generalization of TV.

The TF transform $\mathbf{W}$ can be extended to the multilevel by diluting the masks to ω_i^l such that

$$\begin{aligned}
\omega_0^l &= \frac{1}{4}[1\ \underbrace{0\cdots0}_{2^l-1}\ 2\ \underbrace{0\cdots0}_{2^l-1}\ 1],\\
\omega_1^l &= \frac{\sqrt{2}}{4}[1\ \underbrace{0\cdots0}_{2^l-1}\ 0\ \underbrace{0\cdots0}_{2^l-1}\ -1],\\
\omega_2^l &= \frac{1}{4}[-1\ \underbrace{0\cdots0}_{2^l-1}\ 2\ \underbrace{0\cdots0}_{2^l-1}\ 1].
\end{aligned}$$

Similar to the uni-level TF, define $\mathbf{x}^l = \omega_0^l * \mathbf{x}^{l-1}$, $\mathbf{x}^0 = \mathbf{x}$ and

$$\mathbf{M}_j^l\mathbf{x}^l = \frac{1}{\sqrt{3}}\begin{bmatrix}\omega_j^l * \mathbf{x}_x^l\\ \omega_j^l * \mathbf{x}_y^l\\ \omega_j^l * \mathbf{x}_z^l\end{bmatrix}, \forall j = 0,\cdots,2, \forall l = 1,\cdots L.$$

Then TF transform $\mathbf{W}$ with level L is

$$\mathbf{W}\mathbf{x} = \left[\underbrace{\mathbf{M}_1^1\mathbf{x}^1\ \mathbf{M}_2^1\mathbf{x}^1}_{\texttt{1st level}}\ \cdots\ \underbrace{\mathbf{M}_1^l\mathbf{x}^l\ \mathbf{M}_2^l\mathbf{x}^l}_{l\texttt{-th level}}\ \cdots\ \underbrace{\mathbf{x}^L\ \mathbf{M}_1^L\mathbf{x}^L\ \mathbf{M}_2^L\mathbf{x}^L}_{L\texttt{-th level}}\right], \tag{4}$$

and its adjoint $\mathbf{W}^T$ is defined as

$$\mathbf{W}^T(\mathbf{y}) = \mathbf{x}^L + \sum_{l=1}^{L}\sum_{j=1}^{2}\mathbf{M}_j^l\mathbf{x}^l,\ \texttt{for}\ \mathbf{y} = \mathbf{W}\mathbf{x} \tag{5}$$

Similarly, Eqs (4) and (5) are a generalization of TV to multilevel, and it keeps the framelet features such as $\mathbf{W}^T(\mathbf{W}\mathbf{x}) = \mathbf{x}$. With the TF regularization, Eq (1) becomes

$$\mathbf{x} = \arg\min_{\mathbf{x}}\frac{1}{2}\|\mathbf{A}\mathbf{x} - \mathbf{y}\|_2^2 + \lambda\|\mathbf{W}\mathbf{x}\|_1. \tag{6}$$

The TF regularization term is defined as the isotropic shrinkage TF norm [27]:

$$\lambda\|\mathbf{W}\mathbf{x}\|_1 = \sum_{l=1}^{L}\sum_{j=1}^{2}\lambda_{l,j}\|\mathbf{M}_j^l\mathbf{x}^l\|_1 + \lambda_{L,0}\|\mathbf{x}^L\|_1. \tag{7}$$

Optimization algorithm. The TF regularization (7) is the summation of L_1-norm. To solve the non-differentiable L_1 minimization problem (6), we choose the alternating direction method of multipliers (ADMM) [41] or the so-called Split Bregman method [42]. In general it is difficult to solve the L_1-regularized minimization problem because it has non-differentiable L_1 term. The basic idea of ADMM is to split L_1 and L_2 components by introducing auxiliary

variables **d**, and **v**. Eq (6) becomes

$$\mathbf{x} = \arg\min_{\mathbf{x},\ \mathbf{d},\ \mathbf{v}} \lambda\|\mathbf{d}\|_1 + \frac{1}{2}\|\mathbf{A}\mathbf{x}-\mathbf{y}\|_2^2 + \frac{\mu}{2}\|\mathbf{W}\mathbf{x}-\mathbf{d}+\mathbf{v}\|_2^2, \tag{8}$$

which can be split into three steps:

- **Step 1:** $\mathbf{x}^{n+1} = \arg\ \min_{\mathbf{x}} \frac{1}{2}\|\mathbf{A}\mathbf{x}-\mathbf{y}\|^2 + \frac{\mu}{2}\|\mathbf{W}\mathbf{x}-\mathbf{d}^n+\mathbf{v}^n\|_2^2$
- **Step 2:** $\mathbf{d}^{n+1} = \arg\ \min_{\mathbf{d}}\|\mathbf{d}\|_1 + \frac{\mu}{2}\|\mathbf{W}\mathbf{x}^{n+1}-\mathbf{d}+\mathbf{v}^n\|_2^2$
- **Step 3:** $\mathbf{v}^{n+1} = \mathbf{v}^n + \mathbf{W}\mathbf{x}^{n+1} - \mathbf{d}^{n+1}$

Because of the decoupled form, step 1 is the sum of two differentiable L_2-norm terms. Thus, we can efficiently solve it from its optimal condition by the conjugate gradient method. Note that TF is more computationally efficient than TV due to $\mathbf{W}^T\mathbf{W} = I$. Step 2 can be solved efficiently using the TF shrinkage formula [28]. Step 3 is in its explicit form, thus it is easy to implement.

Experiments

Data acquisition. The multislice helical CT reconstruction quality was evaluated using the American College of Radiology (ACR) CT accreditation phantom (Data Spectrum Corporation. Model: ECT/DLX/P) and the Rando phantom. Siemens SOMATOM Definition 64-slice helical CT scanner was used to generate the helical CT projection data. Details of the scan parameters for ACR phantom were as follows: Various voltage parameters with effective mAs, $\mathrm{CTDI}_{\mathrm{vol}}$, and DLP are described in Table 1. For every voltage level, there was a 3.05 *s* scan time, 0.5 *s* gantry rotation time, and 64 * 0.6 mm collimation with z-flying focal spot. The helical pitch is set to be $p = 1$, with 2304 projections per rotation. Image volume resolution is: 2 *mm* slice thickness and $0.9766 \times 0.9766\ mm^2$ axial resolution. The whole image volume has $512 \times 512 \times 88$ voxels. A 21.6 cm inside diameter cylindrical ACR phantom is used. Parameter details for the Rando phantom scan were as follows: 120kV with 350 effective mAs are used. There was a 17 *s* scan time and 20 * 0.6 mm collimation with z-flying focal spot. The helical pitch is set to be $p = 1$, with 4608 projections per rotation. Image volume resolution is: 4 *mm* slice thickness and $0.9766 \times 0.9766\ mm^2$ axial resolution. The whole image volume has $512 \times 512 \times 53$ voxels.

Quantitative metrics. To evaluate the performance of the proposed algorithm quantitatively in comparison to FDK and the Katsevich algorithm, four different quantitative metrics are selected. The Universal Quality Index (QUI) measures the intensity similarity between the reconstructed and true images. Image noise is measured by Signal-to-Noise Ratio (SNR) and Contrast-to-Noise Ratio (CNR). These two metrics quantify the noise level of the reconstructed images. The Modulation Transfer Function (MTF) is used to evaluate the resolution of the reconstructed images.

Image similarity—Universal Quality Index (UQI). The Universal Quality Index (UQI) [43] was measured to evaluate the similarity between the reconstructed and true images. We considered the image from the scanner to be the true image. Given the ROI within the reconstructed and true images, the associative mean of the image μ, the variance and covariance of μ with the true image $\mu_{\mathtt{true}}$ over the ROI are denoted as $\bar{\mu}$, σ^2, and $\mathtt{Cov}(\mu, \mu_{\mathtt{true}})$, respectively. The definition of UQI is given as

$$\mathtt{UQI} = \frac{4\ \mathtt{Cov}(\mu, \mu_{\mathtt{true}})}{\sigma^2 + \sigma^2_{\mathtt{true}}} \frac{\bar{\mu}\cdot\bar{\mu}_{\mathtt{true}}}{\bar{\mu}^2 + \bar{\mu}^2_{\mathtt{true}}}.$$

Table 1. Scan parameters with different voltages.

voltage (kV)	Effective mAs	$CTDI_{vol}$(32cm) (mGy)	DLP (mGy-cm)
80	178	3.30	66.3
100	165	6.51	130.8
120	161	10.84	217.7
140	153	15.78	316.8

https://doi.org/10.1371/journal.pone.0210410.t001

The UQI measures the intensity similarity between two images, and its value ranges [0, 1]. A UQI value close to 1 indicates a better level of similarity between the reconstructed and true images. We chose two ROIs: The whole ACR phantom body on slices 10 and 50. We calculated the UQI scores for all three methods under comparison.

Image noise—SNR and CNR. To evaluate the quantitative noise level of the reconstructed images, we chose two different metrics, SNR and CNR. The definitions are as follows.

$$\mathrm{SNR} = \frac{\bar{\mu}_{\mathrm{ROI}}}{\sigma_{\mathrm{ROI}}}$$

$$\mathrm{CNR} = \frac{|\bar{\mu}_{\mathrm{ROI}} - \bar{\mu}_{\mathrm{ROI}_{\mathrm{air}}}|}{\sqrt{\sigma^2_{\mathrm{ROI}} + \sigma^2_{\mathrm{ROI}_{\mathrm{air}}}}}$$

where σ_{ROI} and $\sigma_{\mathrm{ROI}_{\mathrm{air}}}$ refer to the standard deviations and $\bar{\mu}_{\mathrm{ROI}}$ and $\bar{\mu}_{\mathrm{ROI}_{\mathrm{air}}}$ refer to the mean pixel value in a ROI inside and the background of the phantom, respectively. We chose four Regions Of Interest (ROI) to compare the reconstructed images from all three methods with that from the scanner. For convenience, the CT numbers are normalized with 1 as the maximum.

Image resolution—MTF. The Modulation Transfer Function (MTF) [43, 44] is calculated to measure resolution of the reconstructed images. An Edge Spread Function (ESF) was obtained along the profile of the red line on Fig 1. The Line Spread Function (LSF) was achieved by differentiating the ESF. The MTF was obtained from the Fourier transformation of the LSF. Normalization was performed as MTF(0) = 1.

Results

Evaluations with low-dose data

Four evaluations metrics were compared on the different dosage levels of 80, 100, 120, and 140 kVs. A different x-ray source has a different effective dosage (see Table 1). We chose two slices for the evaluation process, slices 10 and 50. Figs 1 and 2 show the results for slices 10 and 50, respectively. For both figures, from left to right, each column shows the reconstructed images from the scanner, by FDK, Katsevich, TV, and TF algorithms. Each row consists of reconstructed images from different kVs: (a_j)'s are from 80kV, (b_j)'s are from 100 kV, (c_j)'s are from 120 kV, and (d_j)'s are from 140 kV, for all $j = 0, \cdots, 4$. The red circles on Fig 1 indicate specific ROIs; ROI1, ROI2, ROI3, and $\mathrm{ROI}_{\mathrm{AIR}}$ for the computation of SNR and CNR. ROI 1, ROI2, and ROI3 are the interior of the small circles inside the ACR phantom. The red line in (a_0) is the ROI for the edge spread function, used for calculating MTF. The set of interiors of the small red circles on the 50-th slice, the (a_0) of Fig 2, is set as a ROI4 and the rest of the area except ROI4 inside of the phantom is set to the $\mathrm{ROI}_{\mathrm{AIR}}$ for the computation of the SNR and

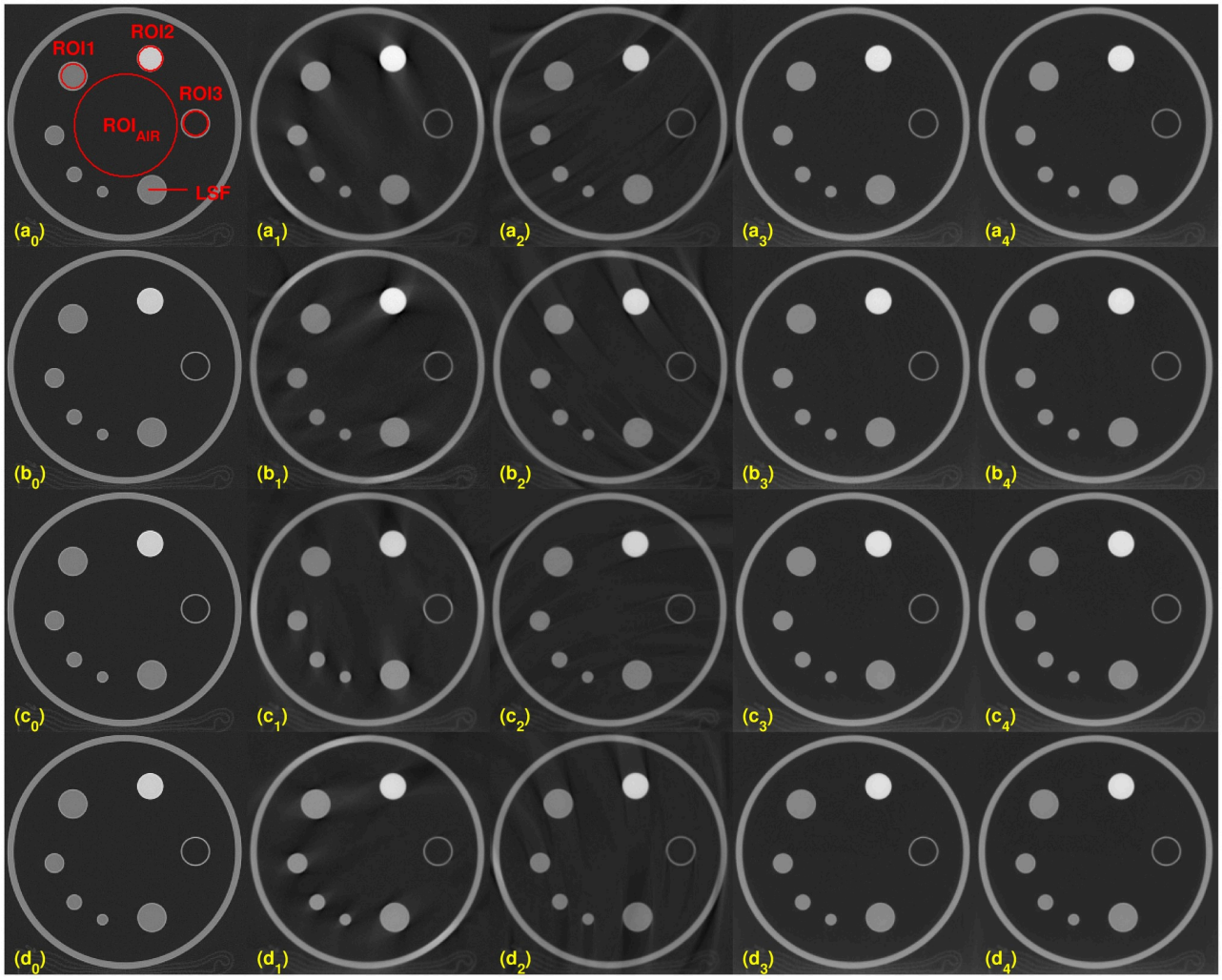

Fig 1. Illustrated reconstructed images with varying kVs on the slice number 10. (a_0): Image from the scanner. Red circles indicate ROI's: ROI1, ROI2, ROI3 and ROI_{AIR}. The red line is used to compute the LSF and MTF. Each row has reconstructed images at different kVs, (a_j): 80kV, (b_j): 100kV, (c_j): 120kV, and (d_j): 140 kV, for all $j = 0 \cdots 4$. Each column has reconstructed images from different reconstruction algorithms: (X_0): scanner, (X_1): FDK, (X_2): Katsevich, (X_3): TV, and (X_4): TF for all letters X = a, b, c or d.

https://doi.org/10.1371/journal.pone.0210410.g001

CNR of ROI4. As illustrated in the Figs 1 and 2, the images from TV and TF reconstruction algorithms give clear images compared to FDK and Katsevich results.

Quantitative evaluation results are shown in Figs 3–5. For computing the UQI, images from the scanner were treated as true. Two ROIs for the UQI are set as the whole ACR phantom on the slices 10 and 50. The left bar plot of Fig 3 shows the result of the UQI in three different algorithms of the ROI on th 10th slice. The right plot shows the UQI result of slice 50. For both plots, the TF reconstruction method achieved the closest value to 1, which means the TF reconstructed image was the most similar to the scanner results. To evaluate the noise level of the reconstructed images, Fig 4 shows the SNR and CNR results at the various dosage levels. The plots on the top row((a)-(d)) are the results of SNR over the ROI1, ROI2, ROI3, and ROI4. Note that each ROI has different y-range, since different ROI has different noise level. ROIs are defined in Figs 1 and 2. CNRs on the ROI1-ROI4 are illustrated in Fig 4(e)–4(h). TF and TV algorithms achieved the high CNR and SNR on the four ROIs at all dosage levels,

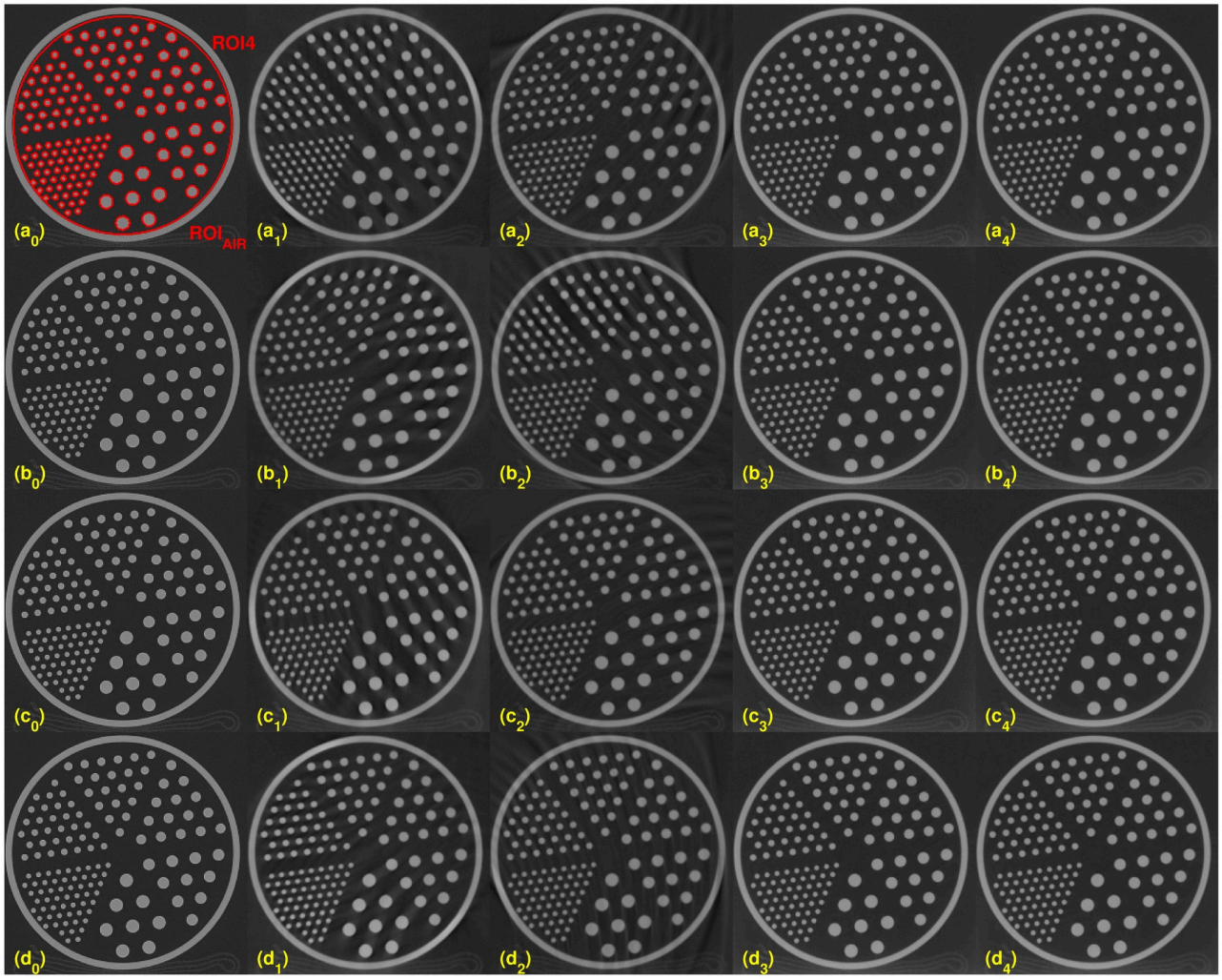

Fig 2. Comparison of the reconstruction algorithms with varying kVs on the 50-th slice. ROI4 is the set of the interiors of the small red circles. ROI_{AIR} is defined as the air part inside the phantom on slice 50-th. Each row has reconstructed images at different kVs, (a_j): 80kV, (b_j): 100kV, (c_j): 120kV, and (d_j): 140 kV, for all $j = 0 \cdots 4$. Each column has reconstructed images from different reconstruction algorithms: (X_0): scanner, (X_1): FDK, (X_2): Katsevich, (X_3): TV, and (X_4): TF for all letters X = a, b, c or d.

https://doi.org/10.1371/journal.pone.0210410.g002

except in one case: The SNR on ROI3 at 120 kV. TF and TV algorithms are comparable. TF achieved the highest value on ROI3, but TV did on ROI4.

Fig 5 shows the MTF curves of the results reconstructed by FDK, Katsevich, TV and the TF algorithm. Over all voltage levels, TF algorithms got the best resolutions than the other algorithms. But the MTF curve gives no big difference in various voltage levels.

Overall, quantitative evaluation results with various dosage show results of TF and TV are competitive.

Evaluations with sparse-view data

To evaluate with sparse-view performance, we fixed the dose level at 100kV. Images were reconstructed at four different sampling steps, 1, 4, 8, and 16. The full view data has 2304 views per 360˚. Sampling step 4 was achieved by taking 576 data uniformly per 360˚. Similarly, sampling steps 8 and 16 were achieved with 288 and 144 views per 360˚, respectively. For sampling

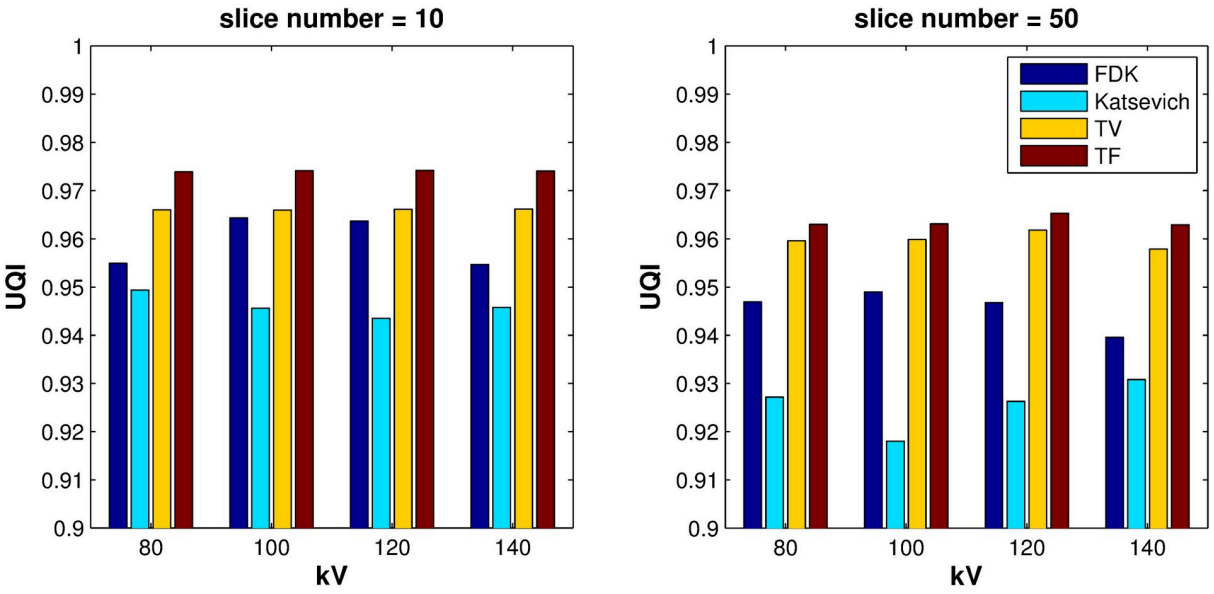

Fig 3. Image similarity measure: Bar plot of the UQIs of the different reconstruction algorithms over various dosage levels. (a): UQI on the 10-th slice, (b): UQI on the 50-th slice.

https://doi.org/10.1371/journal.pone.0210410.g003

step 4, it is equivalent that both the rotation speed and the table movement are four times faster than those of sampling step 1. The results of the reconstruction images with different view-angles are shown in Figs 6 and 7. The images (a_0) and (b_0) are from the scanner on both figures. From the top to the bottom rows, images are reconstructed CT images by sampling steps 1, 4, 8, and 16. Each column shows images from a different reconstruction algorithm. From left to right, each column consists of images by scanner, FDK, Katsevich, TV and the TF

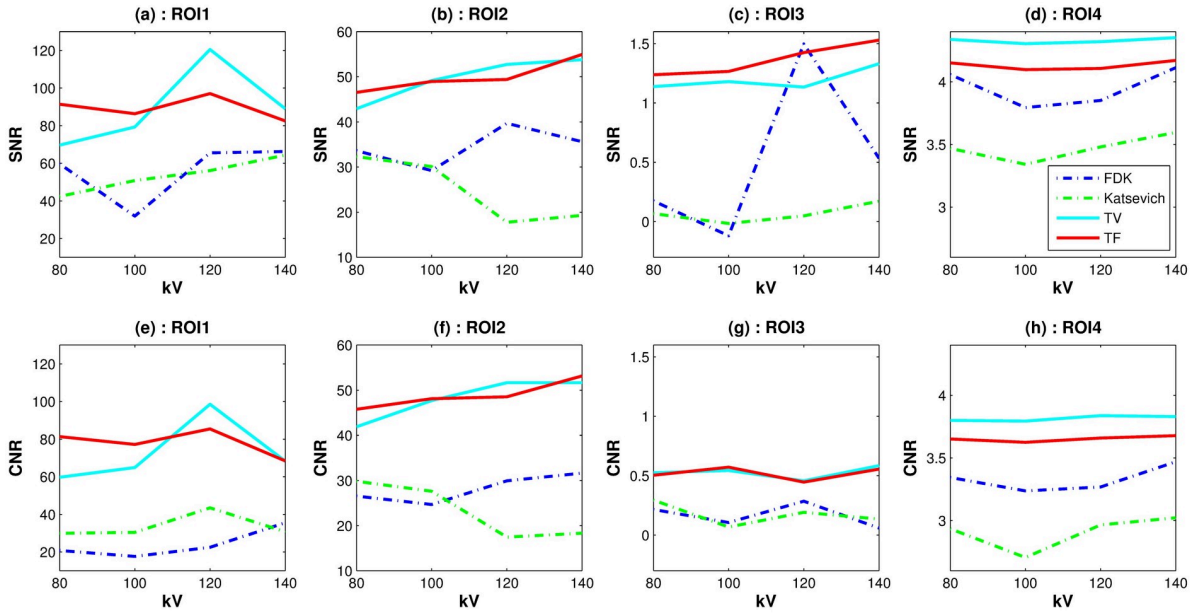

Fig 4. Image noise measures: Plots of SNRs(top row) and CNRs(bottom row) with the different reconstruction algorithms over various voltage levels. The *x*-axis is the dosage level in kV.

https://doi.org/10.1371/journal.pone.0210410.g004

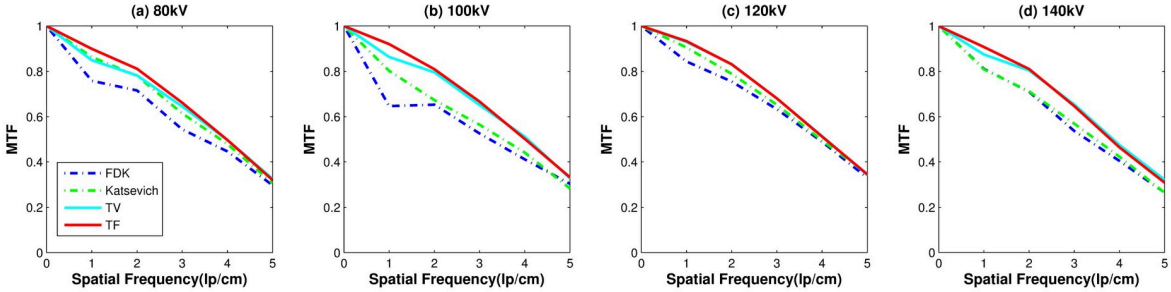

Fig 5. Image resolution measure: Results of MTF curves with the different reconstruction algorithms over various voltage levels. The red line on the Fig 1(a_0) is used to compute LSF and MTF.

https://doi.org/10.1371/journal.pone.0210410.g005

algorithm. As shown in the first row, reconstruction images at sampling step 1 are streak-free for all reconstruction algorithms. However, streaks appeared on the images with FDK and Katsevich for sparse-view data. The last column of the Figs 6 and 7 showed that visually TV and TF reconstruction outperformed other two reconstruction methods. On Figs 6(a_0) and 7(a_0),

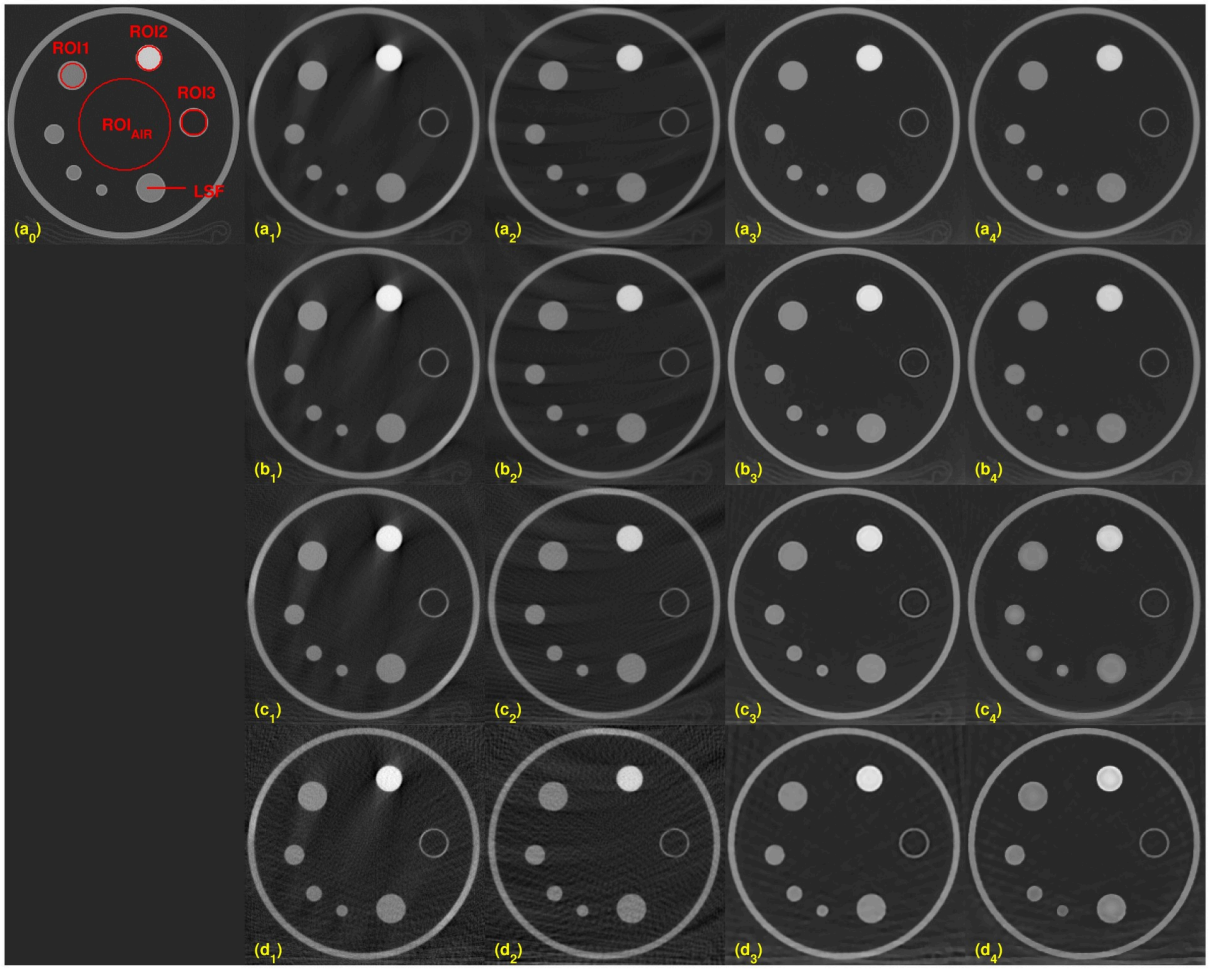

Fig 6. Reconstucted images with various sampling step sizes. From top to bottom, the sampling step size is set to 1, 4, 8, and 16. Each column consists of a different reconstruction algorithm, from left to right, scanner: FDK, Katsevich, TV and the TF algorithm. The image on (a_0) shows the three ROIs, and the red line is set for the computation of LSF for MTF. ROI_{AIR}, ROI of air, is defined to compute the CNR for ROI1-ROI3.

https://doi.org/10.1371/journal.pone.0210410.g006

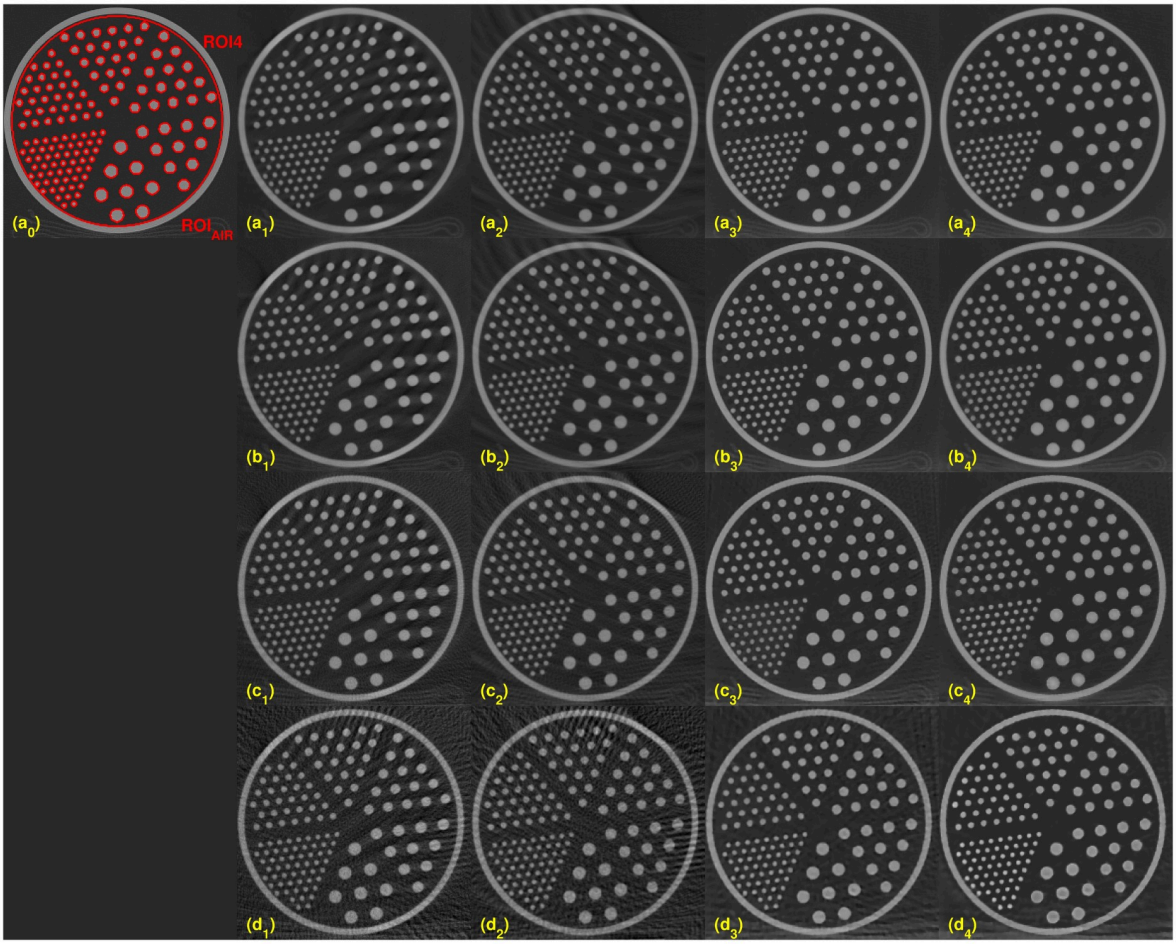

Fig 7. Reconstucted images with various sampling step sizes. From top to bottom, the sampling step size is set to be 1, 4, 8, and 16. Each column consists of a different reconstruction algorithm, from left to right: scanner, FDK, Katsevich, TV and the TF algorithm. The image on (a_0) shows ROI4 and ROI_{AIR}.

https://doi.org/10.1371/journal.pone.0210410.g007

ROI's are defined as in the previous section. Visual comparison between TV and TF is given in the next subsection.

For the quantitative evaluation of similarity between the reconstructed image and the scanner image, we computed the UQI for each slices 10 and 50. The ROI for the UQI is set as the whole phantom area on a given slice. Fig 8 shows the result of UQI with various sampling step sizes. Both plots (a) and (b) show that the TF algorithm achieved the highest value except one case, which means that the image reconstructed using the TF algorithm was the most similar to the scanner image.

For the quantitative evaluation of the noise level of the reconstructed images, we computed the SNR and CNR on ROIs 1–4. Fig 9 shows the SNR and CNR results. Similar to Fig 4, each column in Fig 9 has different y-range. The first row consists of the SNR results for ROI1-ROI4. The second row is the result of the CNR of ROI1-ROI4. Both SNR and CNR indices have a similar pattern. The TF algorithm achieved the highest SNR and CNR except for a few points in ROI2 and ROI4. For the quantitative evaluation of the image resolution, Fig 10 shows MTF curves as described in the previous subsection. The LSF is computed with the ROI indicated in Fig 6(a_0). TV and TF results achieve high resolution than other two algorithms. The TF

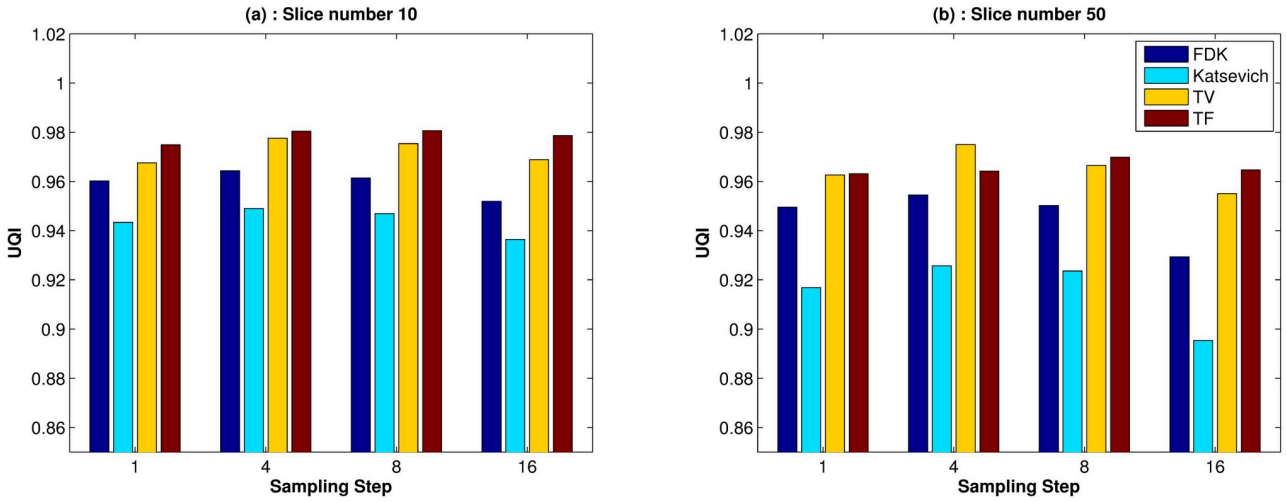

Fig 8. Image similarity measure: UQI results for various sampling step size. *x*- axis is the sampling step size, 1, 4, 8, and 16. *y*- axis is set as the UQI index. (a): UQI bar plot for the 10-th slice. (b): UQI bar plot for the 50th slice.

https://doi.org/10.1371/journal.pone.0210410.g008

algorithm achieved the highest MTF, especially when the fewest sample generated the highest MTF difference among other reconstructed methods.

Comparison with TV

As shown in Figs 1 ~ 7, image qualities of TF and TV are hard to compare. Each quantitative metric shows a slight superiority of TF. To show some good points of the proposed algorithm, we have tested Rando phantom data, which has more realistic and complicated structure than ACR phantom. Rando phantom is scanned and reconstructed with sparse-view as done in the previous subsection. Fig 11 shows the results by TV(top rows) and TF(bottom rows)

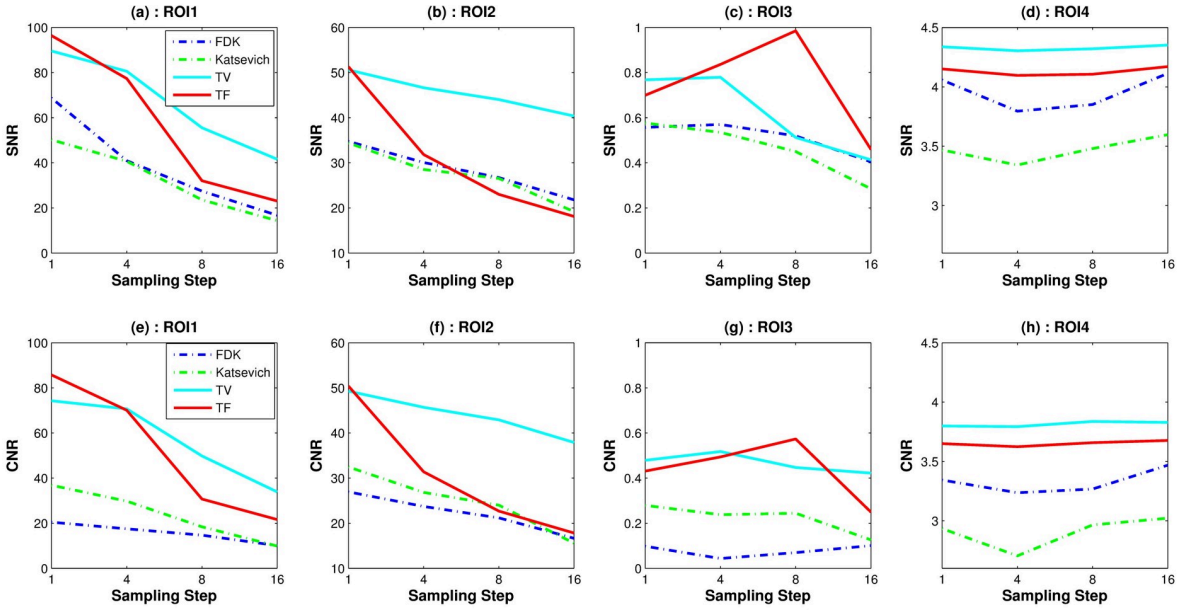

Fig 9. Image noise measures: SNR and CNR results for the various sampling step sizes. First row: SNR result, second row: CNR results.

https://doi.org/10.1371/journal.pone.0210410.g009

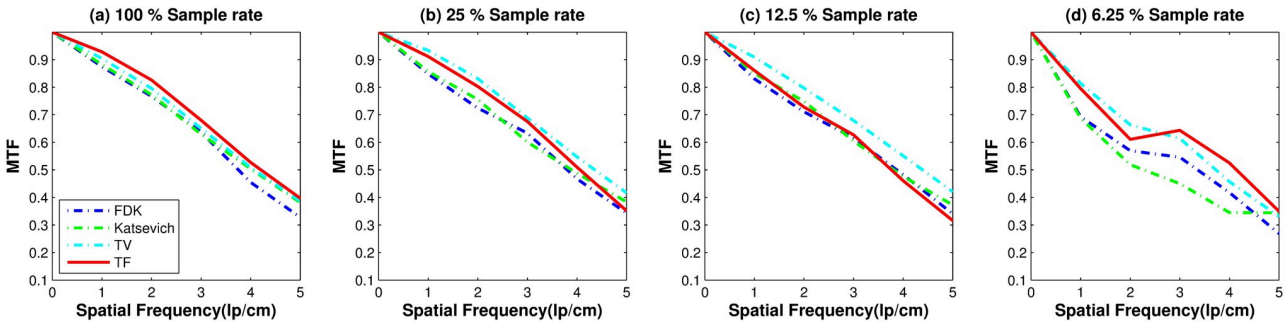

Fig 10. Image resolution measure: Results of MTF curves with different reconstruction algorithms over various sampling levels. The red line on the Fig 6(a_0) is used to compute the LSF and MTF.

https://doi.org/10.1371/journal.pone.0210410.g010

algorithms. The sampling size 1 (which is the right column) results shows similar to each other. But as the step size increases, the TV results are more blurry but clean, while that of TF maintains sharpen edges even with a large step size. Same results can be shown in Fig 6. Fig 12 are same images from Fig 6, TV and TF reconstruction with step 16. Streaking artifacts due to partial projection data are shown less in the TF results. As indicated in red box, TF image has more sharpen edges than that of TV. Overall, we can conclude that TV and TF image qualities are similarly good, but TF has more sharpened edge and less artifacts.

One of the key factor to evaluate iterative algorithms is the reconstruction time. TV and TF elapsed times are summarized in Table 2. TF algorithm requires about 25% less time than TV algorithm.

Discussion and conclusion

To summarize, we have successfully developed a GPU-based TF iterative image reconstruction algorithm for low-dose multislice helical CT, and have shown that the TF method provided

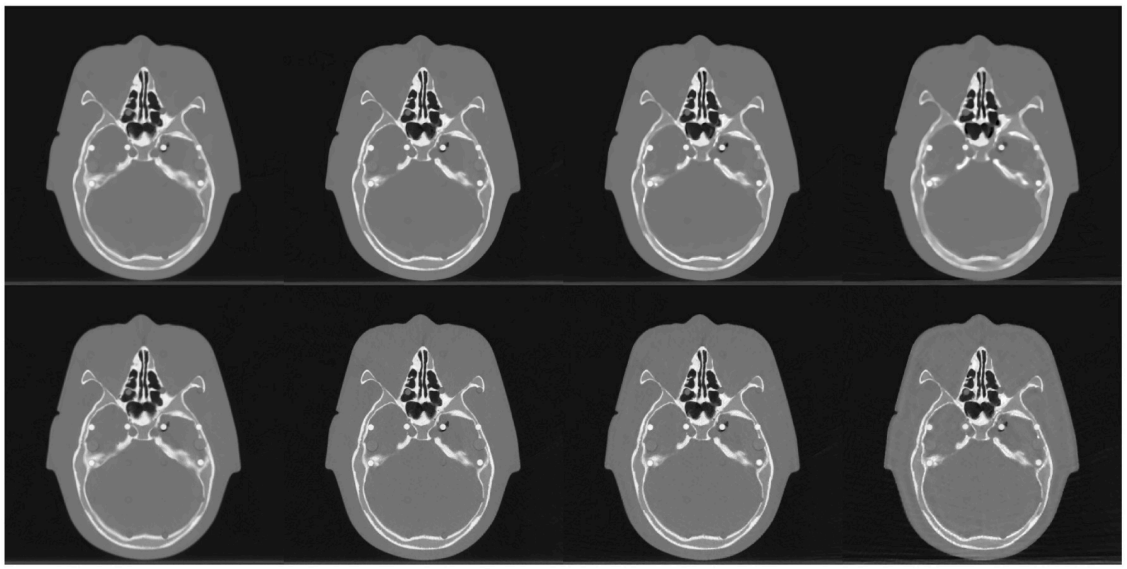

Fig 11. Visual quality comparison: TV(top row) and TF(bottom row). From left to right, reconstruction results by the sampling step size is set to 1, 4, 8, and 16. TV results shows more blurry effect compared to TF results.

https://doi.org/10.1371/journal.pone.0210410.g011

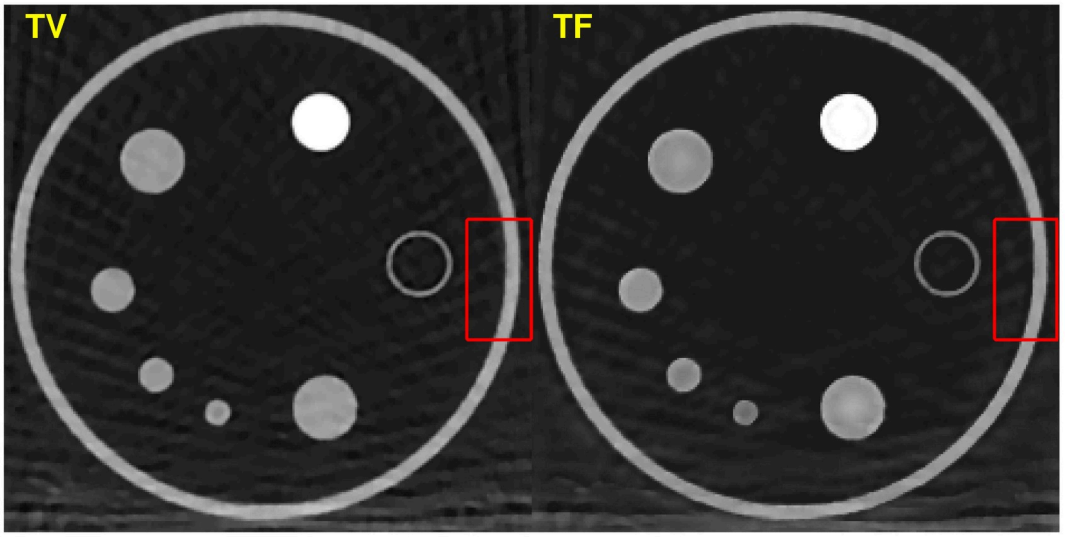

Fig 12. Visual quality comparison: TV(left) and TF(right). TF image has less streaking artifact. As shown in the red box, TF maintain sharpen edge.

https://doi.org/10.1371/journal.pone.0210410.g012

Table 2. TF and TV elapsed time in seconds.

sampling step size	1	4	8	16
TF	18199	4485	1708	718
TV	23303	5674	2692	1429

https://doi.org/10.1371/journal.pone.0210410.t002

improved image quality over the FDK, the Katsevich and TF algorithms when dealing with low-dose and sparse-view data, using UQI, SNR, CNR, and MTF measurements as evaluation metrics. High quality images are reconstructed by the proposed algorithm even with partial view data. TF algorithm is more computationally efficient than that of TV, because of the left-invertibility of the TF transform property [27]. Moreover, TV reconstructed images show more blurry and flattened than TF. The computational complexity of the TF algorithm is O(1), which is the cost of the x-ray transform and its adjoint per parallel thread [27].

Supporting information

S1 Fig. Data related to Fig 1.
(MAT)

S2 Fig. Data related to Fig 2.
(MAT)

S3 Fig. Data related to Fig 6.
(MAT)

S4 Fig. Data related to Fig 7.
(MAT)

S5 Fig. Data related to Fig 11.
(MAT)

Author Contributions

Conceptualization: Haewon Nam, Lei Xing, Hao Gao.

Data curation: Haewon Nam, Keumsil Lee, Ruijiang Li, Bin Han.

Formal analysis: Haewon Nam.

Funding acquisition: Rena Lee.

Methodology: Haewon Nam, Hao Gao.

Resources: Minghao Guo, Bin Han.

Software: Haewon Nam, Minghao Guo, Hengyong Yu, Keumsil Lee, Ruijiang Li.

Supervision: Hengyong Yu, Lei Xing, Hao Gao.

Validation: Haewon Nam.

Visualization: Haewon Nam.

Writing – original draft: Haewon Nam.

Writing – review & editing: Haewon Nam, Rena Lee, Hao Gao.

References

1. Hounsfield G. A method of apparatus for examination of a body by radiation such as x-ray or gamma radiation. US. Patent No. 1283925. 1972.
2. Mori I. Computerized tomographic apparatus utilizing a radiation source. US Patent No. 4630202. 1986.
3. Kalender WA, Seissler W, Klotz E, Vock P. Spiral volumetric CT with single-breathhold technique, continuous transport, and continuous scanner rotation. Radiol. 1990; 176(1): 181–183. https://doi.org/10.1148/radiology.176.1.2353088
4. Feldkamp LA, Davis LC, Kress JW. Practical cone-beam algorithm. JOSA A. 1984; 1(6): 612–619. https://doi.org/10.1364/JOSAA.1.000612
5. Wang G, Lin TH, Cheng PC, Shinozaki DM. A general cone-beam reconstruction algorithm. Med. Img. IEEE Trans. 1993; 12(3): 486–496. https://doi.org/10.1109/42.241876
6. Hein I, Taguchi K, Silver M, Kazarna M, Mori I. Feldkamp-based cone-beam reconstruction for gantry-tilted helical multislice CT, Med. Phys.2003; 12: 3233–3242. https://doi.org/10.1118/1.1625443
7. Zhao J, Lu Y, Jin Y, Bai E, Wang G. Feldkamp-type reconstruction algorithms for spiral cone-beam CT with variable pitch. J. of X-Ray Sci. and Tech. 2007; 15: 177–196.
8. Taguchi K, Aradate H. Algorithm for image reconstruction in multi-slice helical CT. Med. Phys. 1998; 25: 550–561. https://doi.org/10.1118/1.598230 PMID: 9571623
9. Katsevich A. Theoretically exact filtered backprojection-type inversion algorithm for spiral CT. SIAM J. Appl. Math. 2002; 62: 2012–2026. https://doi.org/10.1137/S0036139901387186
10. Katsevich A. Analysis of an exact inversion algorithm for spiral cone-beam CT. Phys. Med. Biol. 2002; 47: 2583–2597. https://doi.org/10.1088/0031-9155/47/15/302 PMID: 12200926
11. Katsevich A. An improved exact filtered backprojection algorithm for spiral computed tomography. Adv. Appl. Math. 2004; 32: 681–697. https://doi.org/10.1016/S0196-8858(03)00099-X
12. Noo F, Pack J, Heuscher D. Exact helical reconstruction using native cone-beam geometries. Phys. Med. Biol. 2003; 48: 3787–3818. https://doi.org/10.1088/0031-9155/48/23/001 PMID: 14703159
13. Yu H, Wang G. Studies on implementation of the Katsevich algorithm for spiral cone-beam CT. J. X-Ray Sci. Technol. 2004; 12: 97–116.
14. Chen GH. An alternative derivation of Katsevich's cone-beam reconstruction formula. Med. phys. 2003; 30(12): 3217–3226. https://doi.org/10.1118/1.1628413 PMID: 14713088
15. Zou Y, and Pan X. Exact image reconstruction on Pi-linew from minimum data in helical cone-beam CT. Phys. Med. Biol. 2004; 49: 941–959.
16. Zou Y, Pan X. Image reconstruction on PI-lines by use of filtered backprojection in helical cone-beam CT. Phys, in Med. and Bio. 2004; 49(12): 2717. https://doi.org/10.1088/0031-9155/49/12/017

17. Ye Y, Wang G. Filtered backprojection formula for exact image reconstruction from cone-beam data along a general scanning curve. Med. Phys. 2005: 32(1); 42–48. https://doi.org/10.1118/1.1828673 PMID: 15719953

18. Ye Y, Zhao S, Yu H, Wang G. A general exact reconstruction for cone-beam CT via backprojection-filtration. Med Img IEEE Trans. 2005; 24(9): 1190–1198. https://doi.org/10.1109/TMI.2005.853626

19. Cho S, Xia D, Pelizzari CA, Pan X. Exact reconstruction of volumetric images in reverse helical cone-beam CT. Med. Phys. 2008; 35(7): 3030–3040. https://doi.org/10.1118/1.2936219 PMID: 18697525

20. Ye Y, Yu H, and Wang G. Gel'fand–Graev's reconstruction formula in the 3D real space. Med. Phys. 2011; 38(S1): S69–S75. https://doi.org/10.1118/1.3577765 PMID: 21978119

21. Thibault JB, Sauer KD, Bouman CA, Hsieh J. A three-dimensional statistical approach to improved image quality for multislice helical CT. Med. Phys. 2007; 34(11): 4526–4544. https://doi.org/10.1118/1.2789499 PMID: 18072519

22. Nuyts J, Man BD, Dupont P, Defrise M, Suetens P, Mortelmans L. Iterative reconstruction for helical CT: a simulation study. Phys. Med. Biol. 1998; 43: 729–737. https://doi.org/10.1088/0031-9155/43/4/003 PMID: 9572499

23. Gordon R, Bender R, Herman GT. Algebraic reconstruction techniques (ART) for three-dimensional electron microscopy and X-ray photography. J. of Theo. Bio. 1970; 29(3): 471–481. https://doi.org/10.1016/0022-5193(70)90109-8

24. Anderson AH, Kak AC. Simultaneous algebraic reconstruction technique (sART): A superior implementation of the art algorithm. Ultrasonic Imaging. 1984; 6: 81–94. https://doi.org/10.1016/0161-7346(84)90008-7

25. Sunnegårdh J, Grasruck M. Nonlinear regularization of iterative weighted filtered backprojection for helical cone-beam CT. IEEE Nuclear Sci. Symposium. 2008; 43: 5090–5095.

26. Yu W, Zeng L. Iterative image reconstruction for limited-angle inverse helical cone-beam computed tomography. Scanning. 2016; 38(1): 4–13. https://doi.org/10.1002/sca.21235 PMID: 26130367

27. Gao H, Li T, Lin Y, Xing L. 4D cone beam CT via spatiotemporal tensor framelet. Med. Phys. Letter. 2012; 39: 6943–6946.

28. Gao H, Qi XS, Gao Y, Low DA. Megavoltage CT imaging quality improvement on TomoTherapy via tensor framelet. Med. Phys. 2013; 40(8): 081919. https://doi.org/10.1118/1.4816303 PMID: 23927333

29. Donoho DL. Compressed sensing. IEEE Transactions on Info. Theory. 2006; 52(4): 1289–1306. https://doi.org/10.1109/TIT.2006.871582

30. Candès EF, Romberg J, Tao T. Robust uncertainty principles: Exact signal reconstruction from highly incomplete frequency information. IEEE Transactions on Information Theory. 2006; 52(2): 489–509. https://doi.org/10.1109/TIT.2005.862083

31. Sidky EY, Kao CM, Pan X. Accurate image reconstruction from few-views and limited-angle data in divergent-beam CT. J. X-Ray Sci. Tech. 2006; 14: 119–139.

32. Chen GH, Tang J, Leng S. Prior image constrained compressed sensing (PICCS): a method to accurately reconstruct dynamic CT images from highly undersampled projection data sets. Med. Phys. 2008; 35(2): 660–663. https://doi.org/10.1118/1.2836423 PMID: 18383687

33. Yu H, Wang G. Compressed sensing based interior tomography. Phys. Med. Bio. 2009; 54(9): 2791. https://doi.org/10.1088/0031-9155/54/9/014

34. Gao H, Cai JF, Shen Z, Zhao H. Robust principal component analysis based four dimensional computed tomography. Phys. Med. Biol. 2011; 56: 3181–3198. https://doi.org/10.1088/0031-9155/56/11/002 PMID: 21540490

35. Gao H, Yu H, Osher S, Wang G. Multi-energy CT based on a prior rank, intensity and sparsity model (PRISM). Inverse Probl. 2011; 27: 115012. https://doi.org/10.1088/0266-5611/27/11/115012 PMID: 22223929

36. Jia X, Dong B, Lou Y, Jiang SB. GPU-based iterative cone-beam CT reconstruction using tight frame regularization. Phy. Med. Biol. 2011; 56(13); 3787. https://doi.org/10.1088/0031-9155/56/13/004

37. Xu Q, Yu H, Mou X, Zhang L, Hsieh J, Wang G. Low-dose X-ray CT reconstruction via dictionary learning. IEEE Trans. Med. Img. 2012; 31(9): 1682–1697. https://doi.org/10.1109/TMI.2012.2195669

38. Flohr TG, Stierstorfer K, Ulzheimer S, Bruder H, Primak AN, McCollough CH. Image reconstruction and image quality evaluation for a 64-slice CT scanner with z-flying focal spot. Med Phys. 2005; 32(8): 2536–2547. https://doi.org/10.1118/1.1949787 PMID: 16193784

39. Gao H. Fast parallel algorithms for the x-ray transform and its adjoint. Med Phys. 2012; 39(11): 7110–7120. https://doi.org/10.1118/1.4761867 PMID: 23127102

40. Dong B, Shen Z. MRA based wavelet frames and applications. IAS Lecture Notes Series, Summer Program on "The Mathematics of Image Processing", Park City Mathematics Institute. 2010; 19.

41. Boyd S, Parikh N, Chu E, Peleato B, Eckstein J. Distributed optimization and statistical learning via the alternating direction method of multipliers, Foundations and Trends® in Machine Learning. 2011; 3(1): 1–122.

42. Goldstein T, Osher S. The Split Bregman method for L1-regularized problems. SIAM J. Imaging Sci. 2009; 2: 323–373. https://doi.org/10.1137/080725891

43. Gao Y, Bian Z, Huang J, Zhang Y, Niu S, Feng Q et al. Low-dose X-ray computed tomography image reconstruction with a combined low-mAs and sparse-view protocol. Optics Exp. 2014; 22(12): 15190–15210. https://doi.org/10.1364/OE.22.015190

44. Judy PF. The line spread function and modulation transfer function of a computed tomographic scanner. Med Phys. 1976; 3(4): 233–236. https://doi.org/10.1118/1.594283 PMID: 785200